Validation of low velocity impact modelling on different stacking sequences of CFRP laminates and influence of fibre failure

Natthawat Hongkarnjanakul, Christophe Bouvet, Samuel Rivallant

To cite this version:

Natthawat Hongkarnjanakul, Christophe Bouvet, Samuel Rivallant. Validation of low velocity impact modelling on different stacking sequences of CFRP laminates and influence of fibre failure. Composite Structures, 2013, vol. 106, pp. 549-559. 10.1016/j.compstruct.2013.07.008 . hal-00858522

HAL Id: hal-00858522
https://hal.science/hal-00858522v1

Submitted on 5 Sep 2013

To link to this article: DOI: 10.1016/j.compstruct.2013.07.008
URL: http://dx.doi.org/10.1016/j.compstruct.2013.07.008

To cite this version: Hongkarnjanakul, Natthawat and Bouvet, Christophe and Rivallant, Samuel *Validation of low velocity impact modelling on different stacking sequences of CFRP laminates and influence of fibre failure.* (2013) Composite Structures, vol. 106. pp. 549-559. ISSN 0263-8223

Validation of low velocity impact modelling on different stacking sequences of CFRP laminates and influence of fibre failure

N. Hongkarnjanakul, C. Bouvet [*], S. Rivallant

Université de Toulouse, ISAE, INSA, UPS, Emac, ICA (Institut Clément Ader), ISAE (Institut Supérieur de l'Aéronautique et de l'Espace), 10 Avenue Edouard Belin, BP 54032, 31055 Toulouse Cedex 4, France

A R T I C L E I N F O

Keywords:
Damage tolerance
Impact behaviour
Finite element analysis (FEA)
Damage mechanics
Fibre failure

A B S T R A C T

This paper presents a validation of low-velocity impact Finite Element (FE) modelling. Based on switching ply location of reference layup $[0_2, 45_2, 90_2, -45_2]_s$ T700GC/M21 laminated plates from Bouvet et al. (2012) [1], twelve possible layups under a constraint of double-ply, mirror-symmetric, balanced, and quasi- isotropic are allowed. However only seven layups are chosen for the study and one of them reveals the importance of longitudinal fibre compressive failure during impact events. Therefore, the second aspect of this work is the introduction of a fibre compressive failure law associated with fracture damage development. This makes it possible to improve the simulation for all seven different layups. Good correspondence is achieved between simulation and experiment for aspects such as delamination areas/shapes and force–displacement responses. The influence of the addition of fibre compressive failure according to fracture toughness in mode I is discussed.

1. Introduction

Low-velocity impact in composite structures has been studying since 1970s. In aeronautics, many researchers have attempted to design optimum structures mainly with respect to their weight. The structures may lose up to 50% of their strength when facing low-velocity impact problems due to accidents during manufacturing or maintenance processes [2]. To cope with this problem, many composite structures are over-designed with a high safety factor to compensate for their low damage tolerance [3], therefore optimised design with Finite-Element Analysis (FEA) becomes necessary and increasingly used in place of experimental tests.

This present work is an extension of Bouvet et al. [1]. An impact FE modelling of UD carbon/epoxy plates has been developed. Using their own model, this team has studied the impact damage in three conventional failure modes, namely fibre failure, matrix cracking, and delamination. The results of impact damage from the model were accurately captured, e.g. force–displacement history, delamination surface, permanent indentation. However, the model was only validated on a single reference layup at a given impact energy. To the authors' knowledge, the literature contains no validation of different impact conditions. Also, in order to enlarge the validity of the reference model, this work will therefore focus on model validation of impact on different stacking sequences, including the presentation of a variety of supplementary post-processing results, e.g. high quality C-scan, and microscopic observation.

The reference stacking sequence is an 8-double-ply, mirror-symmetric, quasi-isotropic laminated plate of T700GC/M21 (carbon/epoxy): $[0_2, 45_2, 90_2, -45_2]_s$, which contains equal numbers of plies in each direction. Note that double-ply is used to facilitate impact damage observation, especially delamination, as well as to reduce calculation time for the simulation. Seven different layups derived from the reference layup were chosen to be tested (cf. Table 1).

Thanks to the different impact behaviours of different stacking sequences, predominant fibre compressive failure was observed in a particular case. Thus, the second point of this work is to improve fibre failure simulation by combining the effect of fibre compressive failure which is often considered as a complex mechanism in the failure of composite structures [4–6].

Some research presents fibre failure models for composites subjected to low-velocity impact. Recently, the energy method seems to be an effective approach to simulate fibre failure or intralaminar ply failure based on the crack band theory from Bažant and Oh [7]. This method uses fracture toughness to dissipate the fracture energy and a characteristic length to avoid the mesh dependent solution. For example, Falson and Apruzzese [8,9] presented the fibre failure which was included in the intralaminar failure mechanism. In their constitutive damage model, the material properties would degrade according to a linear strain-softening law with seven defined damage variables, i.e. fibre failure in tension/compression, matrix failure in tension/compression and three other for the three

---

[*] Corresponding author. Address: ISAE/DMSM, 10 Avenue Edouard Belin, BP 54032, 31055 Toulouse Cedex 4, France. Tel.: +33 (0) 561338968; fax: +33 (0) 561338352.

E-mail address: christophe.bouvet@isae.fr (C. Bouvet).

Table 1
Total possible stacking sequences with seven experimental tested cases.

Layup name	Stacking sequences	Experiment	Remarks
*A*1	$[0_2, 45_2, 90_2, -45_2]_s$	✓	Reference case [1,15]
*A*2	$[90_2, -45_2, 0_2, 45_2]_s$		90° Rotation of A1
*B*1	$[0_2, 45_2, -45_2, 90_2]_s$		
*B*2	$[90_2, -45_2, 45_2, 0_2]_s$		90° Rotation of B1
*C*1	$[0_2, 90_2, 45_2, -45_2]_s$	✓	
*C*2	$[90_2, 0_2, -45_2, 45_2]_s$	✓	90° Rotation of C1
*D*1	$[45_2, 0_2, -45_2, 90_2]_s$	✓	
*D*2	$[-45_2, 90_2, 45_2, 0_2]_s$	✓	90° Rotation of D1
*E*1	$[45_2, -45_2, 90_2, 0_2]_s$	✓	
*E*2	$[-45_2, 45_2, 0_2, 90_2]_s$	✓	90° Rotation of E1
*F*1	$[45_2, 0_2, 90_2, -45_2]_s$		
*F*2	$[-45_2, 90_2, 0_2, 45_2]_s$		90° Rotation of F1

shear directions. This law was assigned as a smeared formulation which assumed constant energy dissipation per unit area in the volume element to generate a mesh-size-independent solution. It was applied and tested for example on an open-hole laminate coupon under compressive loading. Fibre compressive behaviour from their progressive damage law accurately predicted the results of the experiment. Iannucci and Ankersen [3] previously used a similar smeared formulation to develop their low-velocity impact model. They specifically tested this formulation with bi-linear stress–strain damage. They showed that to have a mesh-size-independent FE model, with a given intralaminar fracture energy as an input parameter, the strain at final failure and the evolution of the damage variable may vary with the element size.

Shi et al. [10] added non-linear irreversible shear behaviour to their 3D continuum model of intralaminar failure to simulate permanent indentation for low-velocity impact modelling. Thanks to the energy based criterion and the shear model under progressive damage, permanent indentation was well established. Also, Lopes et al. [11] used energy-based criteria for matrix cracking and fibre failure in 3D plies in their low-velocity impact damage model, with an exponential damage evolution law for the damage propagation. Matrix cracking and fibre failure were accurately predicted. Compression after impact (CAI) modelling was consequently studied by González et al. [12]. According to the same approach for the fibre failure law, they reported that the collapse of the plate was initially triggered by fibre failure, and the CAI strengths for their two tested cases were accurately predicted. Nevertheless, this model was still limited by the calculation time process, e.g. impact and CAI analysis lasted twelve days for the laminate $[45_4, 0_4, -45_4, 90_4]_s$ on 24 CPUs.

As presented above, the modelling of progressive damage with the energy based method could well represent intralaminar damage as a multi-purpose law, e.g. fibre failure, matrix cracking and permanent indentation. In addition to the previous work, Bouvet et al. [1] also used fracture mechanics for their fibre failure modelling. Moreover, they have proposed a new methodology to distribute unequal fracture energy at each integration point (eight integration points in a volume element) depending on the strain magnitude (cf. Section 3.1). Only longitudinal tensile damage for fibre failure was addressed in previous work, whereas the compressive effect would be performed in this paper in the following sections.

However, the value of intralaminar fracture energy, which should be a material property as a model's input, still becomes a sensitive issue since there is no valid standard yet [5,6,4]. Many studies have proposed approaches to measure this value. For example, Soutis and Curtis [6] measured the compressive fracture toughness of T800/924C carbon/epoxy $[0, 90_2, 0]_{3s}$ laminates associated with fibre micro-buckling to be 38.8 N/mm. Also, Pinho et al. [5] used compact compression tests to evaluate the compressive kinking fracture toughness of T300/913 carbon/epoxy laminates. A 79.9 N/mm of fracture toughness was reported. However this value was contested because it was considered only for damage initiation, whereas the propagation was not reliable. Therefore, this current paper will also consider the importance of compressive fracture toughness for damage propagation in order to make the low-velocity impact modelling match the experimental tests according to data available from the literature [6,5].

2. Experimental study and specimen configurations

Impact tests were performed using a drop tower system with a 16 mm diameter, 2 kg impactor, according to the Airbus Industries Test Method (AITM 1-0010). Before impacting the specimen, an optical laser measures the initial velocity. A piezoelectric force sensor is placed inside the impactor to measure contact force during impact. All data are recorded in an oscilloscope. The rectangular specimen measures $100 \times 150\,\text{mm}^2$ simply supported on a $75 \times 125\,\text{mm}^2$ frame, as shown in Fig. 1.

According to the reference case, 8-double-ply layups (0.25 mm nominal ply thickness) of UD carbon- epoxy T700GC/M21 were manufactured based on 0°, 90°, 45° and −45° ply directions. Considering only balanced and mirror-symmetric laminates, switching ply locations makes it possible to have up to 24 configurations. Half of these configurations are symmetric to each other, along the longitudinal axis, i.e. layups $[0_2, 45_2, 90_2, -45_2]_s$ and $[0_2, -45_2, 90_2, 45_2]_s$. Therefore, the 24 potential cases can be reduced to 12 cases studied. However, only seven cases (including the reference case), summarised in Table 1, were experimentally tested, chosen according to the plate's behaviour from analytical calculations and the first-trial simulation. Half of the specimens are derived from a 90° orientation in relation to another specimen. Therefore, to number specimen configurations, the same letter will be used for a laminate and its associated 90° rotation laminate. The quasi-isotropic reference layup A1 contains plies stacked at a constant interface angle of 45°. However, when ply orientation is changed, the interface angle of 90° becomes unavoidable in layups B1, B2, C1, C2, E1 and E2.

3. Numerical modelling

In the previous study, [1] presented a discrete 3D impact model which was simulated with the Abaqus v6.9 explicit solver and a user-defined Vumat subroutine. In their model, three major failure modes observed in composite impact tests were considered: (i) fibre failure in intra-ply, (ii) matrix cracking in intra-ply, and (iii) delamination in inter-ply.

The mesh construction from the previous work was maintained. Positions of nodes are uniformly stacked in row and column for all oriented plies. However, the shapes of mesh are different: 0° and 90° plies are meshed in square shape, while 45° and −45° plies are meshed in parallelogram shape in order to follow the fibre

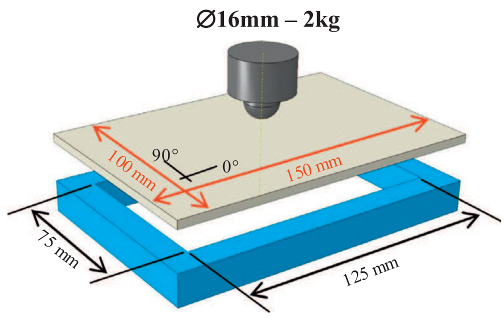

Fig. 1. Impact test setup with the boundary condition.

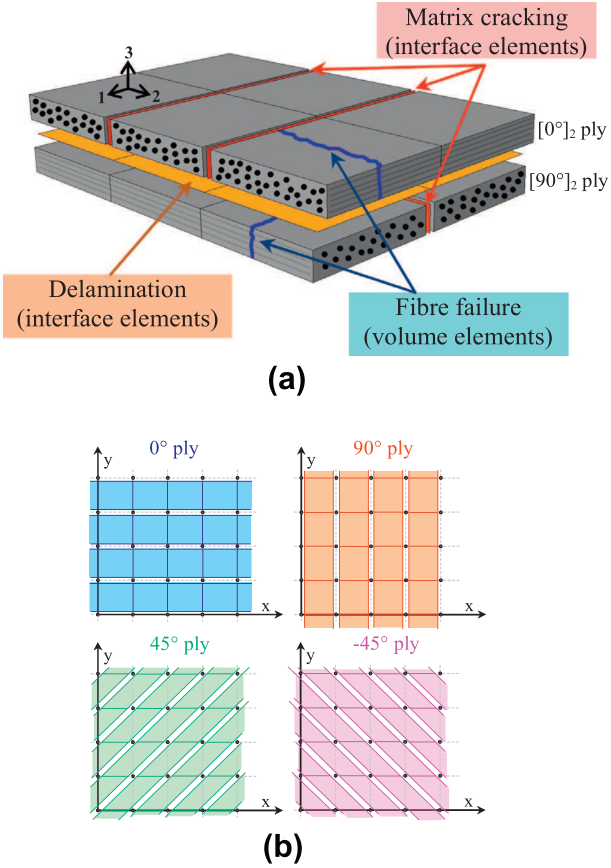

Fig. 2. (a) Modelling of impact damage and element types and (b) mesh shape in each oriented ply [15].

direction and to have coincident nodes in adjacent plies (Fig. 2(b)). The fibre failure was assigned in volume elements *C3D8*, where non-thickness cohesive elements *COH3D8* of delamination are horizontally inserted in-between. Also, vertical non-thickness cohesive elements *COH3D8* are placed between volume element strips in the fibre direction to impose the region of matrix cracking, as shown in Fig. 2(a). Meshing of these three damage types is generated only on half the plate, due to the symmetry consideration. The total number of elements (volume elements and interface elements) is approximately 100,000 elements for each layup configuration. Then, the laminated plate is placed on analytical rigid body supports, and is impacted by a semi-spherical analytical rigid body.

3.1. Modelling fibre failure

Since the fibres primarily break in the fibre direction, the fibre failure mode in this current model means purely longitudinal failure. Shear failure τ_{13} is assumed to have no effect on intralaminar damage, whereas τ_{23} is instead assigned to matrix cracking criterion (cf. Section 3.2). In the experiment, the fibres are locally broken crossing the fibre direction, as illustrated in Fig. 2 and the micrograph in Fig. 8(a). For FE modelling, an alternative method is to dissipate the energy release rate of fibre failure spreading over the volume finite element such as the modelling of [8,1,13,12,11]. Based on crack band theory from [7], a simplified formulation to dissipate the constant energy release rate per unit area in the 3D continuum element can be written as:

$$\int_V \left(\int_0^{\varepsilon_1} \sigma \cdot d\varepsilon \right) \cdot dV = S \cdot G_{Ic}^{fibre} \tag{1}$$

where $G_{Ic}^{fibre}, \varepsilon, \varepsilon_1$ are the fracture toughness for the opening mode (I), the strain in fibre direction, and the strain in fibre direction at final failure, respectively. As seen in Fig. 3(a), these parameters are applicable either in tension ($G_{Ic}^{fibre,T}$ and ε_1^T), or in compression ($G_{Ic}^{fibre,C}$ and ε_1^C). V and S are element's volume and element's cross section normal to fibre direction, respectively. Then, V and S can be reduced in terms of an internal element length l, which is comparable to the FE characteristic length [7,8,10] to make FE model mesh-size independent. Note that the subscripts 0 and 1 denote damage initiation and final failure, respectively.

In addition to distributing the fracture energy over the whole volume element, [1] have proposed a new approach to dissipate the fracture energy defined in terms of eight integration points of each volume element, shown in Fig. 3(b).

3.1.1. Damage initiation

3.1.1.1. Damage initiation of fibre tensile failure. Before reaching the damage initiation state, linear elastic evolution of stress according to longitudinal strain ε at each integration point is defined. As the volume elements can be subjected to bending, the value of strain calculated at nodes can reach the criterion before the strain

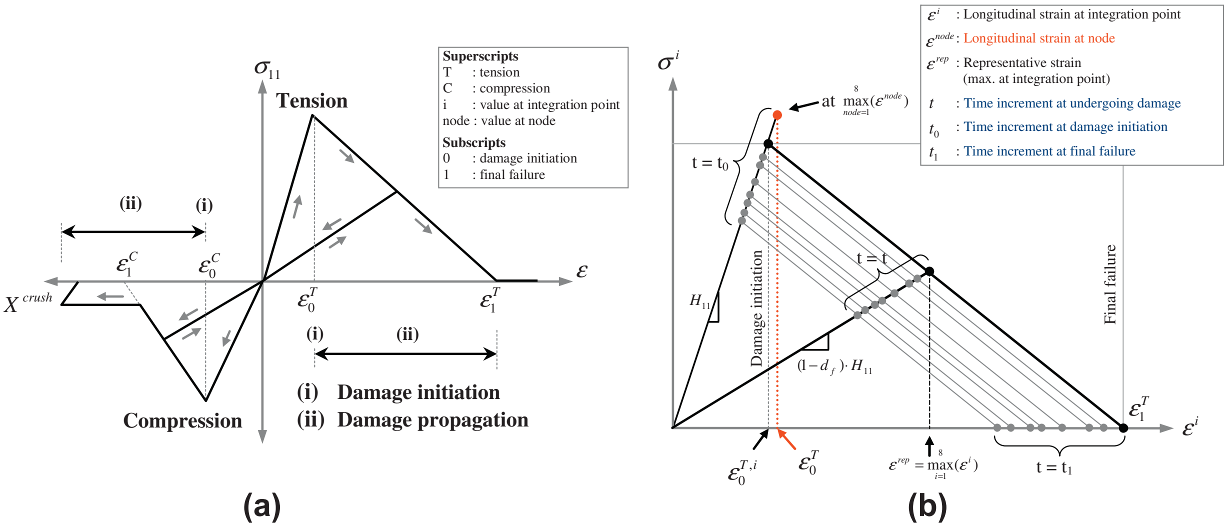

Fig. 3. Constitutive laws of fibre failure in the longitudinal direction: (a) overall fibre failure law with damage initiation and damage propagation under tension and compression and (b) detail of the law when applied to the eight integration points of a 3D element under tension.

Table 2
Mechanical properties of T700GC/M21 unidirectional ply as input in simulation.

Density		1600 kg/m^3
Orthotropic elastic properties [18–20]		
E_1^T	Tensile Young's modulus in fibre direction	130 GPa
E_1^C	Compressive Young's modulus in fibre direction	100 GPa
E_2	Transverse Young's modulus	7.7 GPa
G_{12}	Shear modulus	4.8 GPa
υ_{12}	Poisson's ratio	0.33
Matrix cracking [18,19]		
Y^T	Transverse tensile strength	60 MPa
S^L	In-plane shear strength	110 MPa
Fibre failure [5,14,18,20]		
ε_0^T	Tensile strain in fibre direction at damage initiation	0.016
ε_0^C	Compressive strain in fibre direction at damage initiation	−0.0125
X^{crush}	Longitudinal compressive mean crushing stress	−270 MPa
$G_{Ic}^{fibre,T}$	Fracture toughness for mode *I* in traction	133 N/mm[a]
$G_{Ic}^{fibre,C}$	Fracture toughness for mode *I* in compression	40 N/mm[b]
Delamination [18,21]		
G_{Ic}^{del}	Interface fracture toughness for opening mode (*I*)	0.6 N/mm
G_{IIc}^{del}	Interface fracture toughness for shear mode (*II* and *III*)	2.1 N/mm

[a] Material: T300/913 [5].
[b] Predicted value in this study.

calculated from integration points. Thus, in this model the strain values obtained from eight integration points are computed with the shape function and extrapolated to nodes in order to take into account bending behaviour. Then, the extrapolated strain at each node drives the maximum strain failure criterion defined as:

$$\max_{node=1}^{8}\left(\varepsilon^{node}\right) < \varepsilon_0^T \tag{2}$$

where the superscript *node* means the extrapolation to node and ε_0^T is the tensile strain in the fibre direction at damage initiation, given in Table 2.

When any one of the eight strains calculated at nodes reaches the tensile strain at damage initiation (beyond the limit in Eq. (2)), all stresses at the eight integration points are simultaneously established in the damage initiation state at $t = t^0$, as illustrated in Fig. 3(b).

3.1.1.2. Damage initiation of fibre compressive failure. Similarly to fibre tensile failure, damage initiation of fibre compressive failure can be defined as:

$$\min_{node=1}^{8}\left(\varepsilon^{node}\right) > \varepsilon_0^C \tag{3}$$

where ε_0^C is the compressive strain in fibre direction at damage initiation, given in Table 2.

3.1.2. Damage propagation

3.1.2.1. Damage propagation of fibre tensile failure. The representative strain is the maximum strain of eight integration points which is computed at each time increment. This representative strain will be used for the linear degradation of damage, defined as:

$$\varepsilon^{rep} = \max_{i=1}^{8}\left(\varepsilon^i\right) \tag{4}$$

where the superscript *i* means the value at integration point (fundamentally computed by FE method), and ε^{rep} is the representative strain.

Due to fracture toughness for the opening mode (*I*) in traction $G_{Ic}^{fibre,T}$ i.e. the material input property for the calculation, the fracture energy in volume elements can be dissipated. The tensile final failure strain (ε_1^T) can then be determined by solving Eq. (1).

At each time increment, $\varepsilon_1^{1,T}$ and ε^{rep} will be updated during the undergoing damage propagation state, and the linear degradation of strain-softening can be assigned in terms of the damage variable:

$$d_f = \frac{\varepsilon_1^T\left(\varepsilon^{rep} - \varepsilon_0^{T,i}\right)}{\varepsilon^{rep}\left(\varepsilon_1^T - \varepsilon_0^{T,i}\right)} \tag{5}$$

where $\varepsilon_0^{T,i}$ is tensile strain at damage initiation which is translated to the integration point in order to take into account d_f at the integration points instead of nodes. Note that the damage variable d_f, computed from the representative strain, will be the same for eight integration points, and it will govern the linear degradation behaviour, as illustrated in Fig. 3(b).

3.1.2.2. Damage propagation of fibre compressive failure. Due to the complexity of damage propagation state in compression, parametric study of the longitudinal compressive fracture toughness $G_{Ic}^{fibre,C}$ is performed based on available information from the literature [5,6]. The compressive strain at final failure (ε_1^C) is then determined by solving Eq. (1)similar to the tensile damage. And the representative strain in compression can be defined as:

$$\varepsilon^{rep} = \min_{i=1}^{8}\left(\varepsilon^i\right) \tag{6}$$

with the same fibre failure damage variable, d_f as in tension.

$$d_f = \frac{\varepsilon_1^C\left(\varepsilon^{rep} - \varepsilon_0^{C,i}\right)}{\varepsilon^{rep}\left(\varepsilon_1^C - \varepsilon_0^{C,i}\right)} \tag{7}$$

Additionally, the fibre compressive failure behaviour is slightly more complicated than in tension. Crack initiation in compression is due to the kink band, but when one continues to apply compression, the two sides of the crack come into contact and lead to crushing of packs of fibres. Therefore, the compressive mean crushing stress of T700/M21, X^{crush} proposed by [14] is then applied as a plateau to complete the law. Moreover, the plasticity is also taken into account to prevent compressive strain from returning to zero during the unloaded state, as illustrated in Fig. 3(a).

Then, the stress tensor of orthotropic elasticity in terms of the elastic stiffness matrix and the single fibre damage variable, d_f (both for tension and compression) can be specified as:

$$\begin{Bmatrix} \sigma_{11} \\ \sigma_{22} \\ \sigma_{33} \\ \sigma_{12} \\ \sigma_{13} \\ \sigma_{23} \end{Bmatrix} = \begin{bmatrix} (1-d_f)H_{11} & (1-d_f)H_{12} & (1-d_f)H_{13} & 0 & 0 & 0 \\ & H_{22} & H_{23} & 0 & 0 & 0 \\ & & H_{33} & 0 & 0 & 0 \\ & & & (1-d_f)H_{44} & 0 & 0 \\ & sym & & & (1-d_f)H_{55} & 0 \\ & & & & & (1-d_f)H_{66} \end{bmatrix} \begin{Bmatrix} \varepsilon_{11} \\ \varepsilon_{22} \\ \varepsilon_{33} \\ \varepsilon_{12} \\ \varepsilon_{13} \\ \varepsilon_{23} \end{Bmatrix} \tag{8}$$

where the lamina's stiffness matrix $[H]$ is computed by using the orthotropic elastic properties in Table 2.

3.2. Modelling of matrix cracking

A particular model of matrix cracking is introduced using interface elements (different principal to delamination), between two neighbouring volume elements, which are generated in 1–3 planes, as illustrated in Fig. 2. That means the occurrence of matrix cracking is imposed by the mesh density. The authors assume that it is not necessary to represent the complex matrix microcracks network but only stripes of plies that enable to simulate the changes in load transfers between parts of plies when the matrix is damaged and thus to drive delamination and fibre failures. Therefore a very fine mesh is not necessary. For the same reason, the energy dissipated in matrix cracking is not taken into account in the interface model (brittle failure), but it is nevertheless included in the energy dissipated in the delamination interfaces to keep the energy balance. Matrix tensile failure ($\sigma_{22} > 0$) based according to Hashin's failure criterion is applied to the volume elements. As soon as this criterion (on either one or both neighbouring volume elements) is met, the out-of-plane stresses in the interface elements are set to zero. The two neighbouring volume elements will therefore be independent, meaning that the matrix is broken [15]

$$\left(\frac{\langle\sigma_{22}\rangle^{+}}{Y^{T}}\right)^{2} + \frac{(\tau_{12})^{2} + (\tau_{23})^{2}}{\left(S^{L}\right)^{2}} \leqslant 1 \tag{9}$$

where the subscript 1, 2 and 3 denote the direction of stress according to the volume element. Y^T is the transverse tensile strength and S^L is the in-plane shear strength. In addition to matrix cracking, these interface elements can also model permanent indentation (see more details in [1]).

3.3. Modelling of delamination

The formation of delamination generally relates to matrix cracking [2,1,11]. For this present discrete model, even if there is no coupling parameter of delamination and matrix cracking, the discontinuity still enables this interaction to be represented. Delamination normally occurs between different ply directions. It is therefore simulated in interface elements by joining nodes of upper and lower volume ply elements. Thanks to energy dissipation of fracture mechanics, the delamination criterion is simulated as linear coupling in three modes based on the power law criterion of mixed-mode delamination propagation with the energy release rate: mode *I* is in the thickness direction normal to delamination plane, whilst mode *II* and mode *III* are in the in-plane direction, as explained in [1].

$$\frac{G_I}{G_{Ic}^{del}} + \frac{G_{II}}{G_{IIc}^{del}} + \frac{G_{III}}{G_{IIIc}^{del}} = 1 \tag{10}$$

where G_I, G_{II}, G_{III} represent the energy release rate of delamination in mode *I*, *II* and *III*, respectively. G_{Ic}^{del}, G_{IIc}^{del}, G_{IIIc}^{del} represent the critical energy release rate of delamination in mode *I*, *II* and *III*, respectively.

At the end of the calculation, all layer interface delamination areas are displayed to create a "numerical C-scan". The same colours are used as for the experimental C-scan in order to compare results from simulation with experiments.

4. Experimental validation of the model

In experimental tests, impact energy was expected at 25 J, but in reality the tests were carried out between 24.63 J and 24.82 J for the seven cases studied. To validate the impact damage from the experiments, all seven cases were simulated and compared with the experimental results. Each calculation of impact modelling (5 ms of actual time) lasts approximately 4–5 h on 8 CPUs. According to the previous study [1], impact damage in terms of energy dissipation is mainly separated into two parts, i.e. delamination and fibre failure, as layup D1 shows in Fig. 9(a2). Hence, comparisons between experiments and numerical simulations are presented as follows:

4.1. Delamination

In Fig. 4, delamination is shown. Projected delamination areas are experimentally obtained by ultrasonic C-scan. Thanks to the double-ply stacking configuration, each inter-ply delamination can clearly be distinguished by different colours. Delamination is visibly obvious in the first inter-ply on the non-impacted side (red colour surface in the figures), and the shape at each inter-ply is often oriented in the fibre direction of the lower ply.

The seven experimental tested configurations are compared. The difference between the biggest delamination area (case D2) and the smallest delamination area (case A1) is up to 46% as shown in Fig. 5(a). This difference cannot be attributed only to the effect of stacking sequence, due to parameters coupling when changing the stacking sequence:

- Stiffness of the panel: switching the order of stacking sequences will not affect the membrane stiffness, while the bending stiffness is changed. For example, the laminates C2 is stiffer than C1 and, as a consequence the elastic response during impact is different. The stresses due to bending of laminate C2 are higher than in any other configurations, thus a compression fibre failure is expected. (cf.Section 4.2.2).
- Boundary condition: [16] showed the importance of boundary condition in composite subjected to impact loading when designing real laminated structures near stiffeners of aircraft structures. In this study, except the laminates A1 and C1, the delamination tip is very close to the boundary conditions, which makes it difficult to conclude on the study of influence on extent of damage.

Numerical simulation results show excellent delamination shape comparisons to the experiments for all seven cases. The margin of error between experimental determination of the delamination area and the simulation is within 20%. This margin of error is acceptable since there are many factors affecting the delamination results, for example the quality of experimental C-scans, or uncertainty concerning the values of the parameters of the inputs in modelling, e.g. G_{Ic}^{del}, G_{IIc}^{del}.

Another advantage of numerical simulation on delamination is the possibility of separating delamination in each interface and being able to determine the sum of the delamination areas.

Fig. 5(a) shows that the projected delamination and the total delamination (sum of each interface) follow the same trend.

4.2. Fibre failure

Fibre failure is normally difficult to study experimentally, especially during the impact event. However, microscopic observation, X-ray techniques after impact, or de-ply techniques [17] are probably also effective methods to study it. In this work, we simply observe fibre failure using 2 methods:

4.2.1. Major load drop (studied using either the force–displacement curve or the force–time curve)

Fibre failure can be determined from the major load drop from history curves as presented in Fig. 4. At this energy level (25 J), the major load drop obviously appears in case D1 and D2 in experiment (see Fig. 9(a) for case D1), as well as in numerical simulation. This phenomenon is probably due to fibre tensile failure rather than fibre compressive failure which will be detailed in Section 5.1.

4.2.2. Fibre failure crack on impacted surface (visual inspection)

An apparent long crack on the upper surface (impacted side) across the fibre direction is visible only in case C2, as shown in Fig. 6. In order to investigate the cause of this crack, the specimen C2 was cut for microscopic observation. As presented in Fig. 7, disconnected longitudinal fibres at the impacted side, as well as some small debris from the kink band between the disconnected fibres are observed. The formation of these fibres is similar to fibre micro-buckling/kinking in Fig. 8(b), which could confirm the appearance of the fibre compressive failure. However, rupture modes

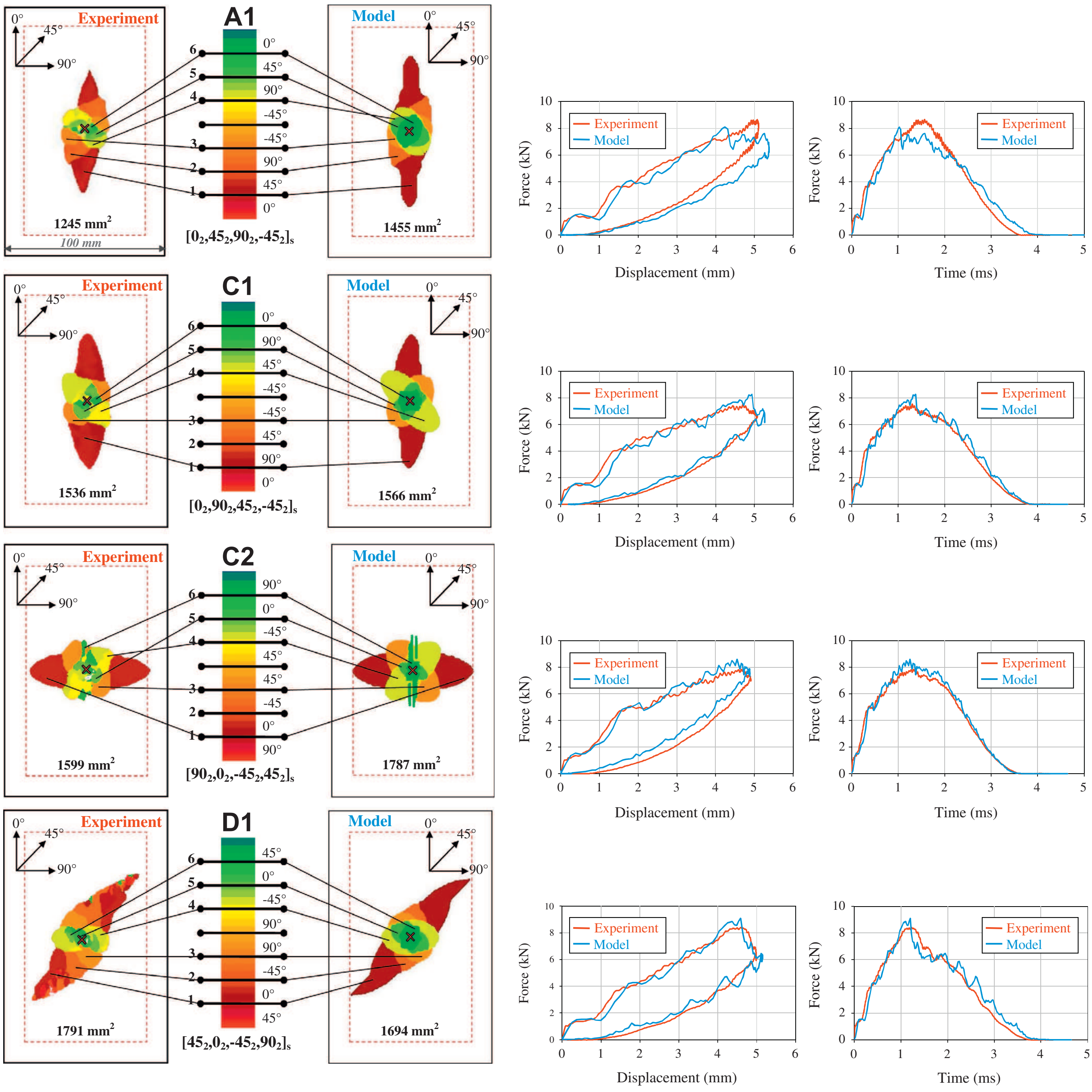

Fig. 4. Comparison between experimental and numerical C-scan for delamination areas, force–displacement curves, and force–time curves of 25 J impact tests.

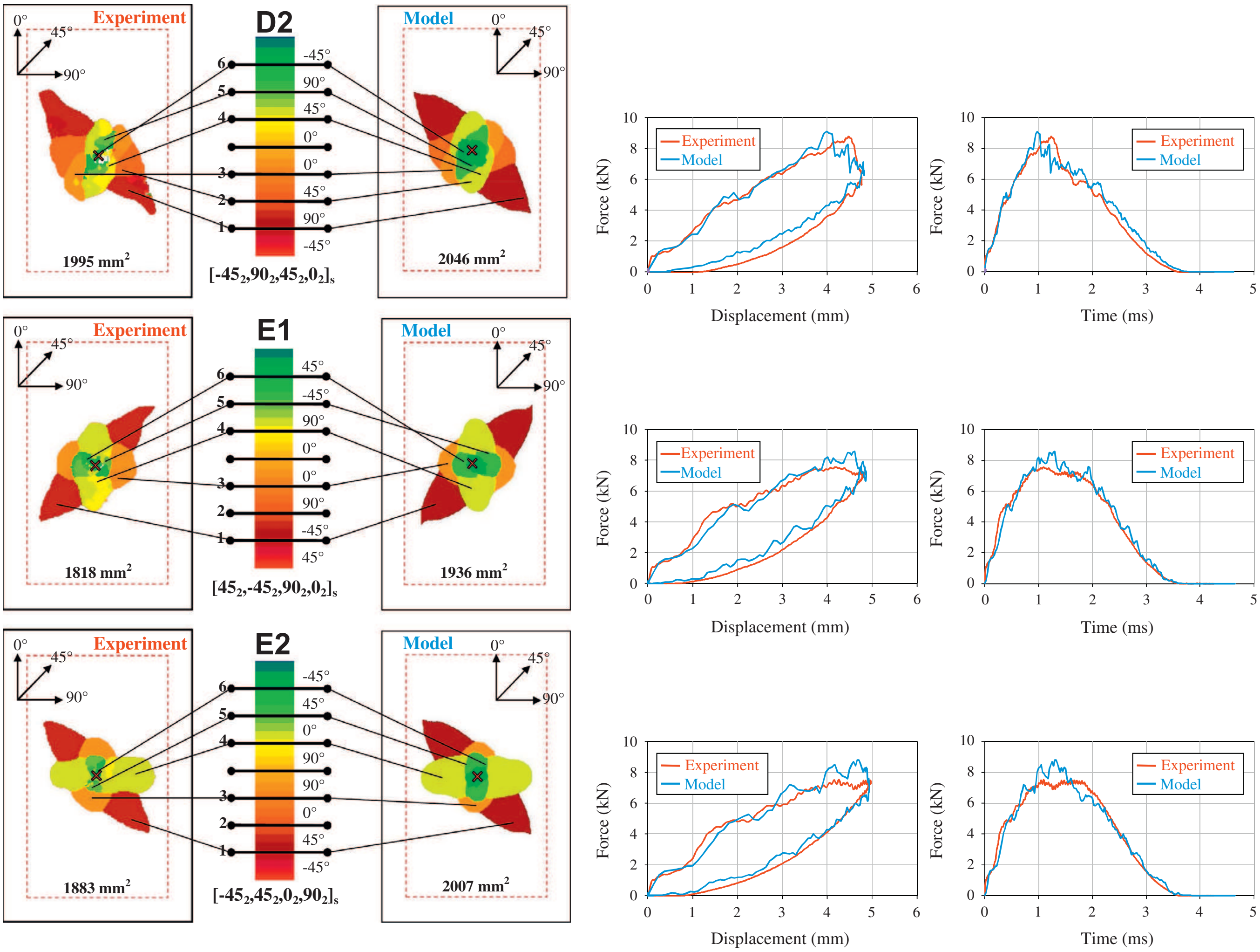

Fig. 4 (*continued*)

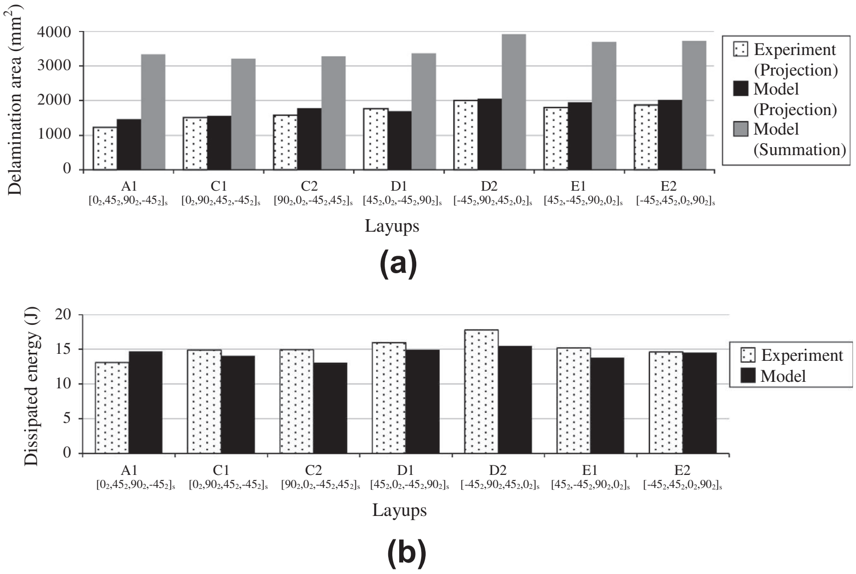

Fig. 5. Experiment-model comparison of seven different layups: (a) delamination area and (b) energy dissipation.

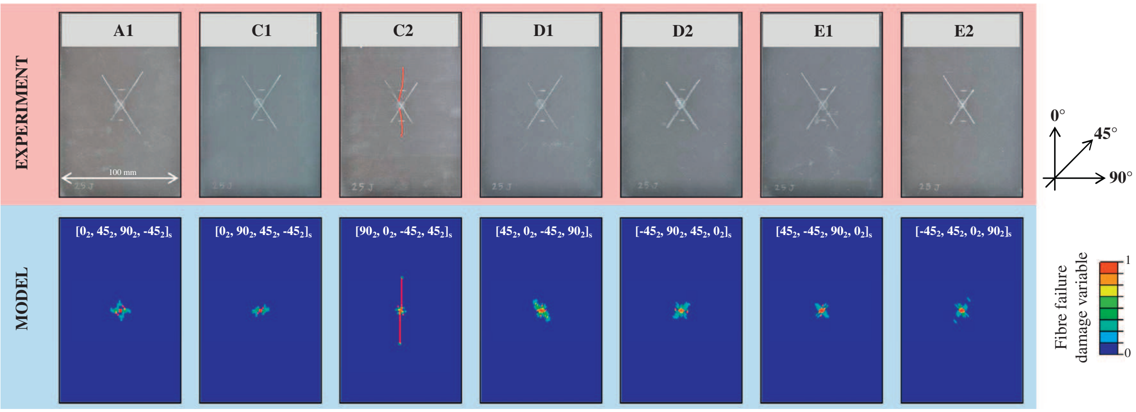

Fig. 6. Fibre compressive failure on the upper surface of different layups in both experiment and simulation.

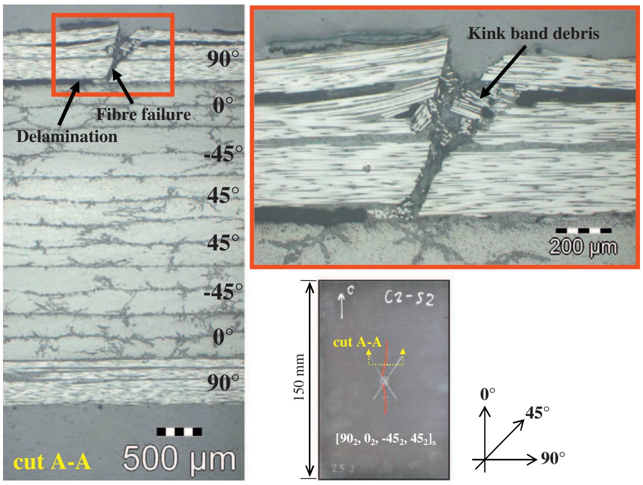

Fig. 7. Microscopic observation of fibre compressive failure of specimen C2 after impact.

from the two images might be slightly different because the fibre compressive failure in Fig. 8(b) involved internal confined plies, whereas in Fig. 7 fibre compressive failure from case C2 was exterior.

To validate the numerical simulation, as seen in Fig. 6, case C2 shows fibre failure in terms of the fibre failure damage variable similar to the noticeable crack in the experimental observation. The detail of fibre compressive failure in this simulation is discussed in Section 5.2.

4.3. Force–displacement history and global impact response

This section again demonstrates that this present model is robust and applicable even if the stacking sequence is changed. The force–displacement and force–time history in Fig. 4 show good agreement in terms of maximum force, maximum displacement and global evolution of impact response. The simulation accurately represents the load drop due to fibre failure as mentioned before, as well as the energy dissipation. The error between the experiment and the simulation of these seven tested cases is less than 12%, as shown in Fig. 5(b).

5. Discussion of failure mechanisms in simulation

5.1. Fibre tensile failure mechanism

According to the previous numerical studies [1], although only fibre tensile failure behaviour was studied in the fibre direction, force response during the impact event was fairly well corroborated with the experimental results. This may therefore imply that fibre tensile failure is predominant for longitudinal failure. Consequently, the same fibre tensile failure law is maintained in this case. In fact, fibre tensile failure appeared at the beginning of the impact event but it was not apparent until a dramatic load drop was recorded. This can be an indicator to identify fibre failure which is confirmed by the simulation, presented in case D1 in Fig. 9.

The dissipation of energy in fibre failure mode, especially on the non-impacted side: ply 2nd, 3rd and 4th plies, suddenly increased. This was simultaneous with the major load drop, precisely in Fig. 9(a1–a3). In addition, the number of elements for fibre failure visibly increased after the major load drop. The number of elements with fibre tensile failure is about 30% more than in fibre compressive failure, which may be induced by the tension from the plate's deflection, as presented in Fig. 9b1–b2.

5.2. Fibre compressive failure mechanism

Some fibre damage was visible after the specimen was impacted, but it does not appear in all cases, as shown in Fig. 6. C2

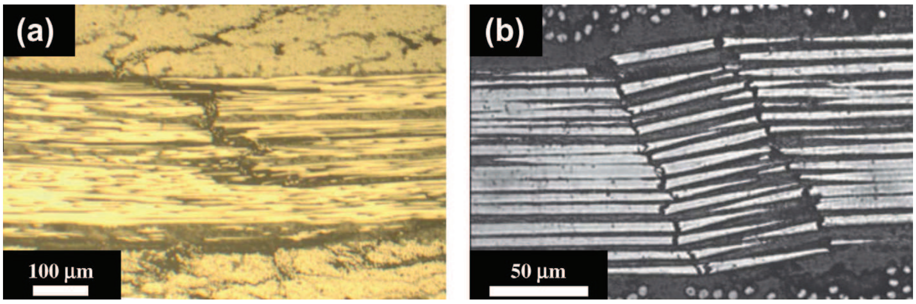

Fig. 8. Micrograph of: (a) fibre tensile failure in the specimen after impact and (b) fibre micro-buckling/kinking formation in CFRP laminate [5].

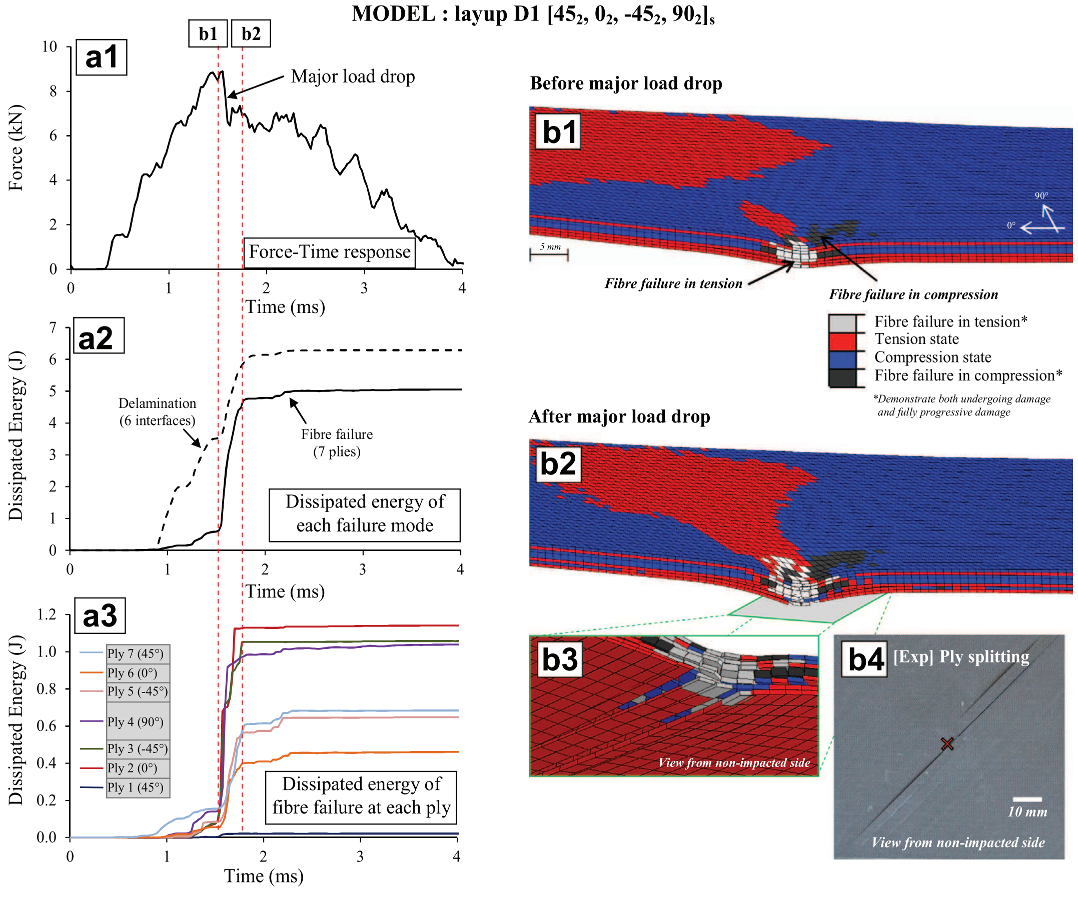

(a) **(b)**

Fig. 9. Simulation on layup D1 for: (a) synchronisation of force and energy dissipation; (b1 and b2) fibre failure states before and after the major load drop; (b3 and b4) ply splitting.

is an interesting layup, having 90° plies on the exterior, lying in the small edge direction of the boundary condition. This observation led to improvement of the model by adding the effect of fibre compressive failure which is a key objective of this paper.

As mentioned previously, fibre failure in this simulation is based on fracture energy, therefore an accurate value of fracture toughness is essential. Before obtaining accurate corroboration between the simulation and the experiment as presented in preceding sections, a parametric study of fibre compressive law and fracture toughness was performed, according to values from the literature. The first value tested for fracture toughness in compression was $G_{Ic}^{fibre,C} = 10\ \text{N/mm}$. The result clearly shows the damage variable of fibre compressive failure on the upper surface in case C2, but in the force–displacement curve, the load drop is still overestimated, as seen in Fig. 10(a). In addition to this inaccuracy, other cases (A1, C1, D1, D2, E1 and E2) have an overestimation of fibre compressive failure as well, for example layup E2 as seen in Fig. 10(b). Then, $G_{Ic}^{fibre,C} = 79.9\ \text{N/mm}$ of T300/913 [5] was tried. This shows a better delamination area according to experimental results with a bigger delamination interface on the impacted side, but fibre compressive failure is underestimated for all seven configurations. Therefore, the value of $G_{Ic}^{fibre,C}$ between 10 and 79.9 N/mm should be considered. $G_{Ic}^{fibre,C} = 40\ \text{N/mm}$ was taken and it could give very accurate results according to experiments in terms of both fibre compressive failure on the upper surface, load drop in force–displacement and delamination shape as shown in Figs. 6, 10(a), and 10(b).

Certainly changing $G_{Ic}^{fibre,C}$ directly affects fibre compressive failure. It should be noted that to obtain these accurate results, the value of $G_{Ic}^{fibre,C} = 40\ \text{N/mm}$ is assigned in the model using the trade-off method. This value is in accordance with the fracture toughness of T800/924C from [6] which is in the same material family as the T700GC/M21 material studied in this work. Nevertheless, further work to determine the fibre compressive failure fracture toughness value of T700GC/M21 is currently in progress. The following stage to determine the residual strength after impact, known as CAI, will be performed based on the same law of impact test fibre compressive failure in this study.

5.3. Coupling between failure modes

The validity of the model is broadened. Thanks to the discontinuity of the particular meshing and independent material law among three failure modes (without coupling parameter), this present model is able to show very good interactions.

- Coupling among fibre failure, matrix cracking, and delamination: As seen in the view of the non-impacted side in Fig. 9(b3), splitting of the lowest ply, induced by matrix cracking and delamination, rather than fibre failure mode, is found. This shows accordance with the experimental observation, as shown in Fig. 9(b4).
- Coupling between fibre failure and delamination: Fibre compressive failure is accompanied by delamination as reported in [5,6]. Microscopic section of specimen C2 in Fig. 7 confirms this phenomenon. In addition, numerical modelling of layup C2 also reveals this interaction, which is in agreement with the experiment, as shown in Fig. 11.

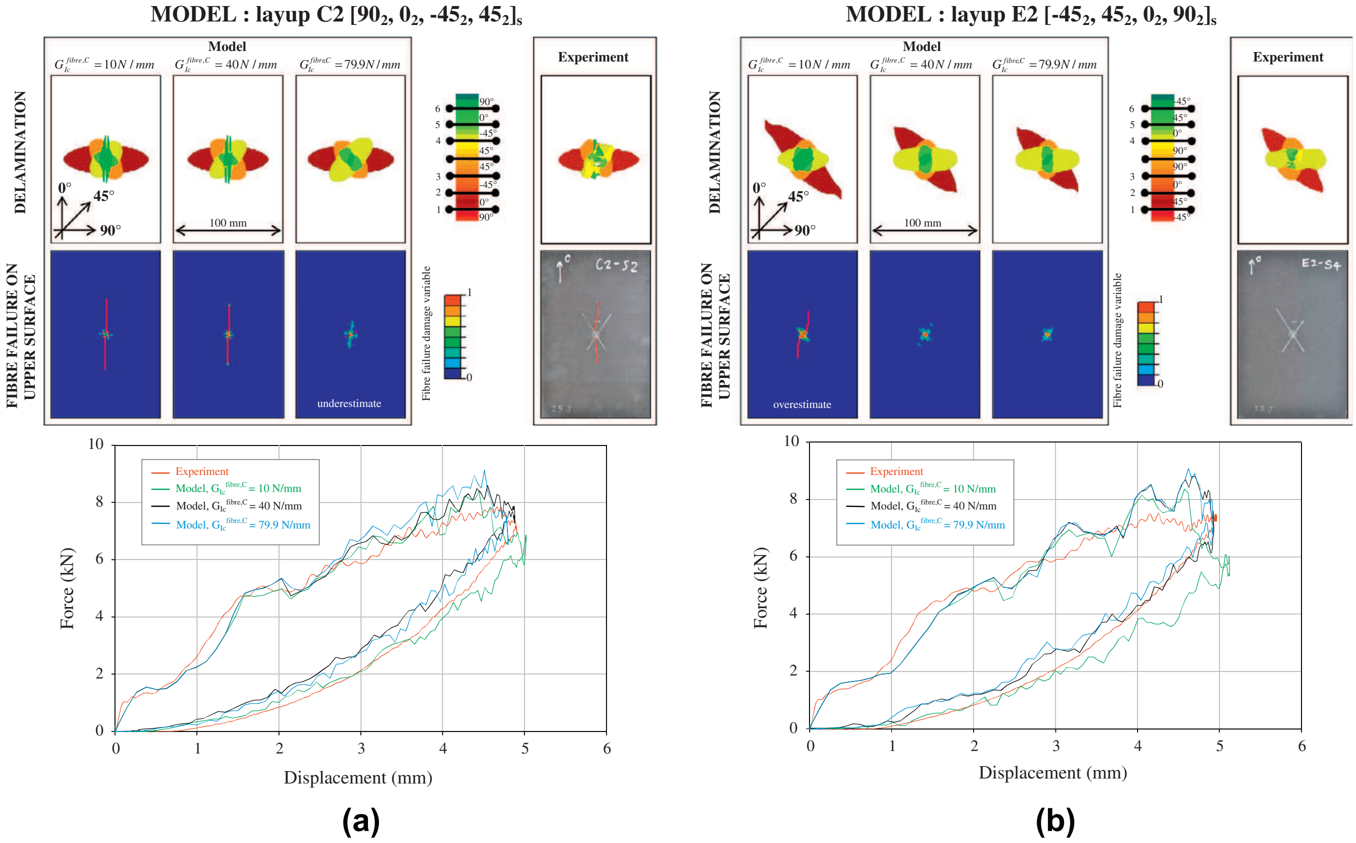

Fig. 10. Validation of $G_{Ic}^{fibre,C}$ of delamination/fibre compressive failure on the upper surface/force–displacement curve on layups: (a) C2 and (b) E2.

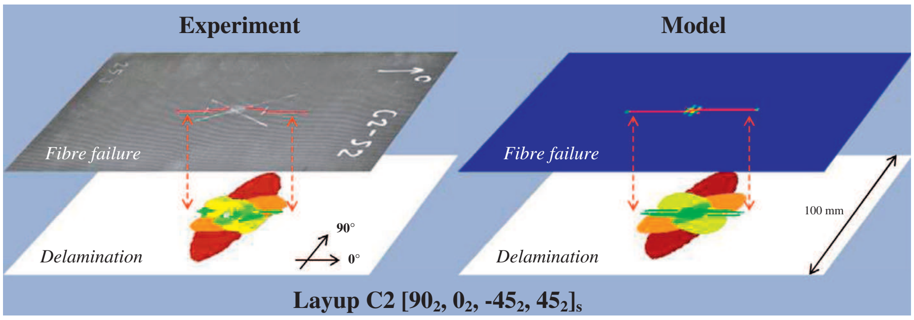

Fig. 11. Demonstration of the coupling between fibre failure and delamination on the upper ply (non-impacted side) of layup C2.

Moreover, global behaviour of the impact response, e.g. coupling of matrix cracking and delamination, force–displacement response, overall delamination area, etc., also needs the interaction between each failure mode. Therefore, a careful trade-off must be made to balance the selected parameters of all impact damage types, in order to obtain an accurate impact simulation.

6. Conclusions

Fibre failure mechanisms have an important role in the response of composite structures subjected to impact. However, in experiments, fibre failures are difficult to observe because of their location inside the laminate, and the fact that they are not as visible as delamination from ultrasonic C-scans.

In this work, we can easily determine the presence of fibre ruptures with the noticeable load drop of force–displacement or force–time curves. This load drop predominates in fibre tensile failure which can occur when the plate is submitted to adequate impact energy. Fibre compressive failure is less well known and is rarely observed during impact tests. In this study, seven layups were experimentally studied, including an interesting case (C2) with a 90° ply on the upper surface of the laminate. Fibre compressive failure was visible in this upper ply after the laminate was impacted.

The fact that compressive fibre failure was observed led to improve the reference model [1]. A new compressive law was implemented. This law is similar to the one already used for fibre rupture under tension, with a dissipation of fracture energy in the volume elements, driven by a damage variable calculated at the eight integration points. Moreover, the effect of crushing in the cracks induced by fibre failure is taken into account with a plateau and a plastic-like law. An identification of the fracture toughness value for compression fibre failure was made by means of a parametric study. The 40 N/mm value is found to be the most appropriate to best describe the observed damage in the C2 laminate.

This new compressive law, applied to the six other laminates, also improves the results of impact simulations on these plates in terms of force–displacement history, force–time history, and delamination.

The current model proves to be quite reliable, and presents a certain number of advantages such as the calculation time (4–5 h/calculation), a relatively limited number of material parameters required, and without any coupling parameters between failure modes.

To widen the validity of this model, other validations such as effect of impact velocity/energy, effect of boundary condition, ply-drops configuration, and sub-laminate/ply grouping are still in progress in order to approach the situations of real aeronautical structures. Thanks to the proposed fibre compressive failure law, modelling of compression after impact (CAI) will soon be continued using the same law.

Acknowledgements

This work was granted access to the HPC resources of CALMIP under the allocation 2012-P1026. The authors also gratefully acknowledge the financial support through the THEOS Operation Training Program (TOTP).

References

[1] Bouvet C, Rivallant S, Barrau JJ. Low velocity impact modeling in composite laminates capturing permanent indentation. Compos Sci Technol 2012;72(16):1977–88.
[2] Richardson MOW, Wilsheart MJ. Review of low-velocity impact properties of composite materials. Compos Part A: Appl Sci Manuf 1996;27A:1123–31.
[3] Iannucci L, Ankersen J. An energy based damage model for thin laminated composites. Compos Sci Technol 2006;66(7–8):934–51.
[4] Laffan MJ, Pinho ST, Robinson P, Iannucci L, McMillan AJ. Measurement of the fracture toughness associated with the longitudinal fibre compressive failure mode of laminated composites. Compos Part A: Appl Sci Manuf 2012;43(11):1930–8.
[5] Pinho ST, Robinson P, Iannucci L. Fracture toughness of the tensile and compressive fibre failure modes in laminated composites. Compos Sci Technol 2006;66(13):2069–79.
[6] Soutis C, Curtis PT. A method for predicting the fracture toughness of CFRP laminates failing by fibre microbuckling. Compos Part A: Appl Sci Manuf 2000;31:733–40.
[7] Bažant ZP, Oh BH. Crack band theory for fracture of concrete. Mater Struct 1983;16(3):155–77.
[8] Falzon BG, Apruzzese P. Numerical analysis of intralaminar failure mechanisms in composite structures Part I: FE implementation. Compos Struct 2011;93(2):1039–46.
[9] Falzon BG, Apruzzese P. Numerical analysis of intralaminar failure mechanisms in composite structures part II: applications. Compos Struct 2011;93(2):1047–53.
[10] Shi Y, Swait T, Soutis C. Modelling damage evolution in composite laminates subjected to low velocity impact. Compos Struct 2012;94(9):2902–13.
[11] Lopes CS, Camanho PP, Gürdal Z, Maimí P, González EV. Low-velocity impact damage on dispersed stacking sequence laminates part II: numerical simulations. Compos Sci Technol 2009;69(7–8):937–47.
[12] González EV, Maimí P, Camanho PP, Turon A, Mayugo JA. Simulation of drop-weight impact and compression after impact tests on composite laminates. Compos Struct 2012;94:3364–78.
[13] Donadon MV, Iannucci L, Falzon BG, Hodgkinson JM, de Almeida SFM. A progressive failure model for composite laminates subjected to low velocity impact damage. Compos Struct 2008;86(11–12):1232–52.
[14] Israr HA, Rivallant S, Barrau JJ. Experimental investigation on mean crushing stress characterization of carbon-epoxy plies under compressive crushing mode. Compos Struct 2013;96:357–64.
[15] Bouvet C, Castanié B, Bizeul M, Barrau JJ. Low velocity impact modelling in laminate composite panels with discrete interface elements. Int J Solids Struct 2009;46(14–15):2809–21.
[16] Faggiani A, Falzon BG. Predicting low-velocity impact damage on a stiffened composite panel. Compos Part A: Appl Sci Manuf 2010;41(6):737–49.
[17] Sztefek P, Olsson R. Tensile stiffness distribution in impacted composite laminates determined by an inverse method. Compos Part A: Appl Sci Manuf 2008;39(8):1282–93.
[18] Prombut P. Caractrisation de la propagation de dlaminage des stratifis composites multidirectionnels. Ph.D. thesis; Universit de Toulouse; 2007 [Type = Phdthesis].
[19] Guillon D. Etude des mécanismes dabsorption dénergie lors de lécrasement progressif de structures composites à base de fibre de carbone. Ph.D. thesis; Universit de Toulouse; 2008 [Type = Techreport].
[20] Tomblin J, Sherraden J, Seneviratne W, Raju KS. A basis and B basis design allowables for epoxy based prepreg TORAY T700GC-12K-31E/#2510 unidirectional tape. Tech. Rep. November; National Institute for Aviation Research. Wichita, KS; 2002.
[21] Vandellos T, Hautier M, Huchette C. A strategy to identify a cohesive zone model coupled with intralaminar damage. In: 14th European conference on composite materials (ECCM/14). Budapest; 2010.